A Novel Group of Dynamin-Related Proteins Shared by Eukaryotes and Giant Viruses Is Able to Remodel Mitochondria From Within the Matrix

Shaghayegh Sheikh,[1,2] Tomáš Pánek,[3] Ondřej Gahura,[1] Jiří Týč,[1] Kristína Záhonová,[1,4,5] Julius Lukeš,[1,2] Marek Eliáš,*[,5] and Hassan Hashimi*[,1,2]

[1]Institute of Parasitology, Biology Centre, Czech Academy of Sciences, České Budějovice, Czech Republic
[2]Faculty of Science, University of South Bohemia, České Budějovice, Czech Republic
[3]Department of Zoology, Faculty of Science, Charles University, Prague, Czech Republic
[4]Department of Parasitology, Faculty of Science, Charles University, BIOCEV, Vestec, Czech Republic
[5]Department of Biology and Ecology, Faculty of Science, University of Ostrava, Ostrava, Czech Republic

***Corresponding authors:** E-mails: marek.elias@osu.cz; hassan@paru.cas.cz.

Associate editor: Christine Orengo

Abstract

The diverse GTPases of the dynamin superfamily play various roles in the cell, as exemplified by the dynamin-related proteins (DRPs) Mgm1 and Opa1, which remodel the mitochondrial inner membrane in fungi and metazoans, respectively. Via an exhaustive search of genomic and metagenomic databases, we found previously unknown DRP types occurring in diverse eukaryotes and giant viruses (phylum *Nucleocytoviricota*). One novel DRP clade, termed MidX, combined hitherto uncharacterized proteins from giant viruses and six distantly related eukaryote taxa (Stramenopiles, Telonemia, Picozoa, Amoebozoa, Apusomonadida, and Choanoflagellata). MidX stood out because it was not only predicted to be mitochondria-targeted but also to assume a tertiary structure not observed in other DRPs before. To understand how MidX affects mitochondria, we exogenously expressed MidX from *Hyperionvirus* in the kinetoplastid *Trypanosoma brucei*, which lacks Mgm1 or Opa1 orthologs. MidX massively affected mitochondrial morphology from inside the matrix, where it closely associates with the inner membrane. This unprecedented mode of action contrasts to those of Mgm1 and Opa1, which mediate inner membrane remodeling in the intermembrane space. We speculate that MidX was acquired in *Nucleocytoviricota* evolution by horizontal gene transfer from eukaryotes and is used by giant viruses to remodel host mitochondria during infection. MidX's unique structure may be an adaptation for reshaping mitochondria from the inside. Finally, Mgm1 forms a sister group to MidX and not Opa1 in our phylogenetic analysis, throwing into question the long-presumed homology of these DRPs with similar roles in sister lineages.

Key words: **dynamin superfamily, Mgm1, mitochondria, *Nucleocytoviricota*, Opa1, protists.**

Introduction

The life of eukaryotic cells relies on extensive membrane dynamics. Diverse membranous structures constantly undergo shape remodeling, fission, and fusion to mediate vital cellular functions like endomembrane trafficking, organelle biogenesis and recycling, and cell division. This whirling is orchestrated by a complex protein machinery that mostly consists of domains assigned to a limited number of conserved families (Rout and Field 2017). Most of these protein families, such as small regulatory GTPases or SNAREs, underpin the dynamics of the autogenously evolved endomembrane system. In contrast, the large GTPase superfamily typified by dynamins is more universal, being also key for the dynamics of the structures that originated by endosymbiosis, that is, mitochondria, plastids (Praefcke and McMahon 2004; Ramachandran and Schmid 2018), and even more recently acquired bacterial endosymbionts (Morales et al. 2023). The importance of the dynamin superfamily in organellar biogenesis and inheritance has been established thanks to functional studies in model organisms. However, it remains uncertain how applicable this knowledge is across the whole breath of the eukaryote diversity.

Here, we focus on the mitochondrion, an organelle established by integration of an alphaproteobacterial endosymbiont prior to the divergence of all currently known eukaryotic lineages. It possesses two membranes that delineate two internal compartments: the intermembrane space situated between the outer and the inner mitochondrial membrane (OMM and IMM, respectively) and the matrix enveloped by the latter. In aerobes, the IMM folds into the matrix, making prominent invaginations called

Article

cristae, which harbor the respiratory chain complexes for generating energy in the form of ATP (Wolf et al. 2019). Semiautonomous mitochondria are passed to the new cell generation by division of preexisting organelles. The central component of the mitochondrial division machinery is the dynamin-related protein (DRP) called Dnm1 in yeast and DNM1L/DRP1 in mammals, which encircles the fission site on the outer leaf of the OMM to eventually sever the double membrane via its GTPase activity (Pernas and Scorrano 2016; Imoto et al. 2020).

However, mitochondrial dynamics goes beyond simple division towards propagation: a constant cycle of fusion and fission among individual organelles plays a critical role in maintaining functional mitochondria during the cell cycle. Like fission, fusion of mitochondrial membranes is also mediated by dynamin superfamily proteins (Pernas and Scorrano 2016). Of these, mitofusins are embedded via transmembrane domains (TMDs) in the OMM and their GTPase domain protrudes outside to mediate OMM fusion. Two other DRPs, optic atrophy 1 (Opa1) and mitochondrial genome maintenance 1 (Mgm1) known primarily from animals and yeast, respectively, localize to the intermembrane space, being present in two forms: as full-size proteins anchored by an N-terminal TMD into the IMM or as soluble cleavage products lacking the N-terminal anchor (Herlan et al. 2003; Anand et al. 2014). Both Opa1 and Mgm1 were shown to mediate IMM fusion and remodeling (Pernas and Scorrano 2016; Ramachandran and Schmid 2018). Interestingly, Opa1 and Mgm1 are each restricted to a small subset of eukaryotes, whereas the distribution of mitofusins overlaps that of the two IMM DRPs (Muñoz-Gómez et al. 2015; Purkanti and Thattai 2015; Sinha and Manoj 2019), raising the question whether other dynamin superfamily proteins play equivalent roles in eukaryotes lacking these well-established mediators of the mitochondrial dynamics. In any case, the nonuniversal distribution of the abovementioned DRPs suggests that they have contributed to morphological and perhaps also functional diversifications of mitochondria (Pánek et al. 2020).

Apart from maintaining membrane homeostasis, certain members of the dynamin superfamily are implicated in cellular defense mechanism targeting viruses, bacteria, and endoparasitic eukaryotes (Kutsch and Coers 2021). However, in an ironic twist, dynamin superfamily members may themselves contribute to pathogen entry and propagation in the host cell. For example, various viruses enter cells via dynamin-dependent endocytosis, making dynamin proteins interesting antiviral targets (Harper et al. 2013). A host-derived DRP was identified as one of the most abundant host-encoded protein copurifying with virions of the giant *Cafeteria roenbergensis* virus (CroV) infecting a marine stramenopile flagellate (Fischer et al. 2014). Although the functional significance of this association is not known, it is conceivable that extensive reorganization of host membranes facilitates viral replication (Ketter and Randall 2019) and may involve recruitment of host-encoded dynamin superfamily proteins. Most recently, a DRP was reported to be encoded directly in the Clandestinovirus genome and suggested to allow the virus to manipulate mitochondria; however, no evidence was presented (Rolland et al. 2021).

Clandestinovirus, as well as CroV, belongs to an intriguing group termed the nucleocytoplasmic large DNA viruses (NCLDVs), recently redefined as the phylum *Nucleocytoviricota* (Koonin et al. 2020). This expansive viral group is characterized by large (~100 kb) to giant (up to ~2.5 Mb) double-stranded DNA genomes encoding up to ~2,500 proteins (Schulz et al. 2022). Perhaps more surprising than their gene richness are the types of proteins encoded by *Nucleocytoviricota* genomes, famously exemplified by components of the translation apparatus, which are otherwise restricted to cellular genomes (Koonin and Yutin 2019). Other notable "cellular" genes found in various *Nucleocytoviricota* viruses include those encoding enzymes of the glycolytic pathway or the tricarboxylic acid cycle (Brahim Belhaouari et al. 2022), the molecular motor myosin (Kijima et al. 2021), actin-related proteins (Da Cunha et al. 2022), or proteins regulating membrane trafficking (Khalifeh et al. 2022). This gene repertoire may facilitate the observed massive rearrangements of the internal host cell architecture for the formation of virus replication foci, referred to as viral factories (Rodrigues et al. 2021). However, details of these interactions are largely unknown.

In our recent review on the morphological diversity of mitochondrial cristae, we pointed out evidence for the uncertain evolutionary relationship between Opa1 and Mgm1, the two DRPs implicated in the IMM fusion and remodeling (Pánek et al. 2020). Our attempt to resolve this controversy led us to discover an unexpected link between the mitochondria and *Nucleocytoviricota*. Specifically, we found a novel DRP type that is shared by *Nucleocytoviricota* viruses and certain protist groups and is targeted into the mitochondrial matrix to remodel the IMM in an unprecedented way. Our findings have interesting functional and evolutionary implications, which are herein discussed.

Results and Discussion

Nucleocytoviricota Encode a Plethora of Diverse DRPs

During reevaluation of the relationship of Opa1 and Mgm1 by a taxonomically comprehensive phylogenetic analysis of the dynamin superfamily, we noticed the existence of diverse DRPs encoded by various representatives, isolated or known only from metagenomic data, of the viral phylum *Nucleocytoviricota*. To examine the occurrence of viral DRP genes on a systematic basis, we searched viral protein sequences available in public databases with a profile hidden Markov model (HMM) built from the seed alignment of the Pfam family Dynamin_N (PF00350), combined with blast searches. Surprisingly, 123 nonredundant sufficiently long significant hits were returned, suggesting a rich repertoire of viral DRPs. The DRP-encoding viruses were all classified in *Nucleocytoviricota*, predominantly in the order

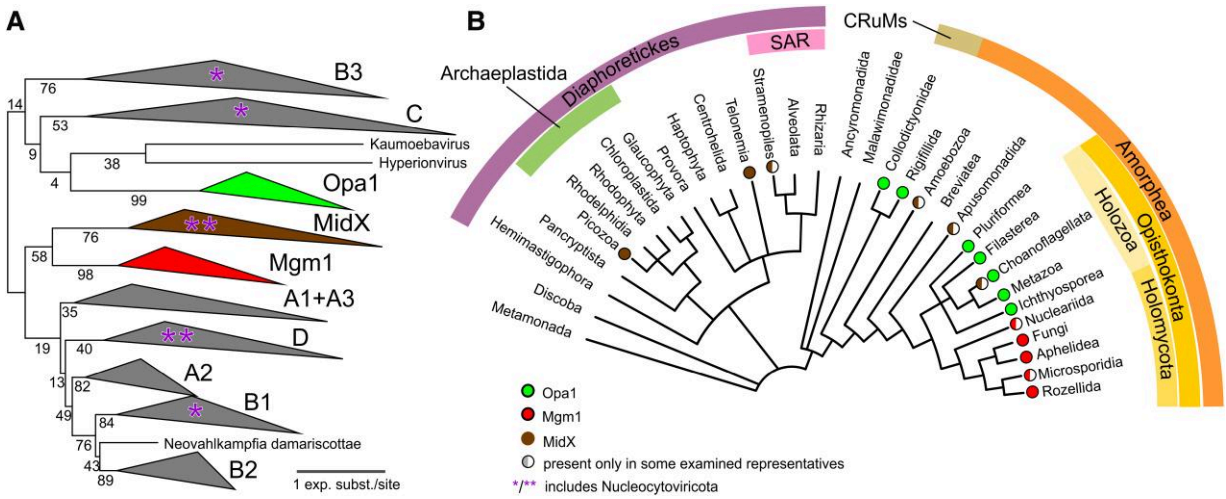

Fig. 1. Revisiting the phylogenetic diversity of the dynamin superfamily identifies novel subgroups. (*A*) Phylogenetic tree inferred with the ML method in IQ-TREE (using the LG4X substitution model and 100 nonparametric bootstraps) from a multiple sequence alignment (527 positions) of a broad selection of DRPs. The final alignment contained 573 sequences with >200 amino acid positions (after trimming). Stable clades are collapsed for simplicity (full version of the tree in supplementary fig. S2, Supplementary Material online). Clades designated A1–3, B1–3, and C are comprised of sequences previously assigned (or related) to DRP classes A, B, and C (Purkanti and Thattai 2015); the D and MidX DRP clades are newly recognized here. Clades containing representatives encoded by *Nucleocytoviricota* viruses are marked with asterisks (**highly represented by viral sequences). (*B*) Phylogenetic distribution of three mitochondrion-targeted DRP types in eukaryotes. The schematic eukaryote phylogenetic tree reflects the most recent phylogenomic studies (Tice et al. 2021; Tikhonenkov, Mikhailov, et al. 2022). Color coding for Opa1, Mgm1, or MidX is provided in the legend on bottom middle. Details on the MidX and Mgm1/Opa1 genes identified are provided, respectively, in supplementary tables S1 and S2, Supplementary Material online.

Imitervirales, and within it in the highly studied family *Mimiviridae*, together with several additional putative families lacking formal names (see supplementary table S1, Supplementary Material online).

We then studied the phylogenetic position of these viral DRPs in the context of a broad data set of DRP sequences from diverse eukaryotes and selected sequences from metagenomes and metagenomically assembled genomes (MAGs). We restricted this analysis to five previously defined classes representing the "core" of the dynamin superfamily, that is, excluding the distantly related mitofusins and bacterial dynamin-like proteins (BDLPs) (Purkanti and Thattai 2015). Preliminary analyses using various sequence subsets, different ways of building and trimming the multiple sequence alignment, and different substitution models resulted in different tree topologies generally exhibiting limited resolution (i.e., low branch support; example shown in supplementary fig. S1, Supplementary Material online). However, 11 groups (clades) were retrieved in most analyses, including the final analysis based on a multiple alignment guided by information from experimentally determined and bioinformatically predicted structural models of reference DRPs (figs. 1 and S2, Supplementary Material online). The groups A1–A3 represent class A dynamins, with the A1 group including some of the best studied DRPs, such as dynamins themselves (involved in endocytosis) or Dnm1/DRP1 mediating fission of mitochondria and peroxisomes. The groups B1–B3 represent class B dynamins, which include (as part of the B2 group) the extensively studied Mx proteins implicated in defense against viruses. Class C dynamins, among others including the DRP5B protein involved in plastid division, formed a single clade in our analyses. The remaining four groups corresponded to Opa1, Mgm1, and two novel groups of DRPs denoted here as MidX (discussed in detail below) and group D dynamins. The latter two groups are particularly enriched with DRPs of viral origin, instances of which are found also within B1 and B3 groups and class C. Some viral DRPs were not reproducibly affiliated to any of the 11 major groups and remain unclassified. The nonmonophyly of the classes A and B observed in our trees warrants further investigations and a possible update of the classification of the dynamin superfamily (Purkanti and Thattai 2015), which is beyond the scope of this study.

Our analyses clearly show that *Nucleocytoviricota* has at their disposal a variety of DRPs that appear to belong to stable, monophyletic clades that could possibly represent functionally specialized DRPs. Given that viral DRPs are interspersed with eukaryotic DRPs within groups B1 and B3 plus class C (see supplementary fig. S2, Supplementary Material online), they were most probably transferred to *Nucleocytoviricota* by horizontal gene transfer (HGT) from various eukaryotes. In contrast, the inferred phylogeny suggests that the whole group D may be originally viral and only later introduced into genomes of a few protist lineages (Ancyromonadida, Haptophyta, and Telonemia) by potentially multiple HGT events (see supplementary fig. S2, Supplementary Material online). The origin of viral representatives of the MidX group is addressed in detail in the subsequent section.

Such a rich repertoire of DRPs in *Nucleocytoviricota* is unexpected, because the only previously reported viral DRP

is encoded by the recently described Clandestinovirus. Named "dynamin 1-like protein" (DNM1-L), it was proposed to influence mitochondrial activities of the host cell; however, no evidence was presented linking the protein to the mitochondrion (Rolland et al. 2021). Indeed, this protein is neither closely related to DRPs with established mitochondrial function (see supplementary fig. S2, Supplementary Material online) nor predicted to be localized to the mitochondrion (see supplementary table S1, Supplementary Material online). Hence, while we cannot completely exclude the possibility that the Clandestinovirus DRP affects mitochondrial physiology, present evidence for this hypothesis is extremely tenuous.

MidX Is a New Group of Putative Mitochondrial DRPs Most Closely Related to Mgm1

Strikingly, the novel MidX group that is enriched with *Nucleocytoviricota* DRPs was consistently placed sister to the Mgm1 group in our analyses, albeit typically with low statistical support (figs. 1, S1, and S2, Supplementary Material online). Given that budding yeast Mgm1 is a mitochondrion-targeted DRP (Herlan et al. 2003; Pernas and Scorrano 2016), we evaluated the subcellular localization of MidX proteins, including the viral representatives, with *in silico* prediction tools. Indeed, an array of prediction software indicates that nearly all MidX proteins (viral or cellular) represented by N-terminally complete sequences possess a mitochondrial targeting signal (MTS) (see supplementary table S1, Supplementary Material online). In contrast, no evidence for mitochondrial localization was seen for virus-encoded DRPs falling outside the MidX group, including DNM1-L from Clandestinovirus (see supplementary table S1, Supplementary Material online). Owing to the putative mitochondrial localization of the novel dynamin superfamily group and the lack of previously characterized members, we named it MidX for *mi*tochondrial *D*RPs of an unknown function.

Given our special interest in the MidX group, we carried out a systematic exploration of various currently available sequence resources to identify as many MidX representatives as possible. Thus, we identified MidX sequences not only in genome or transcriptome assemblies from cultured organisms but also in single-cell genome assemblies, metagenomes, and MAGs. The richest source of MidX sequences proved to be the marine metagenomes and MAGs generated by the Tara Oceans consortium (Delmont et al. 2022). All MidX sequences were manually curated to achieve accuracy of the inferred protein sequences and to define their taxonomic provenance when possible. Altogether, we collected 130 nonredundant MidX sequences, that is, sequences obtained from different eukaryotes, viruses, or environmental samples (see supplementary table S1, Supplementary Material online). To maximize the phylogenetic signal for deeper insight into the phylogenetic relationships within the MidX group, we carried out a separate phylogenetic analysis on a longer sequence alignment obtained by restricting the analysis to all identified MidX sequences plus representative sequences of the most closely related Mgm1 group (see supplementary figs. S2 and S3, Supplementary Material online).

All MidX sequences from cultures, single-cell genomes, and MAGs could be assigned to an identified species or at least to a broader eukaryote taxon, indicating the occurrence of MidX in representatives of six eukaryote lineages: Choanoflagellata, Apusomonadida, Amoebozoa, Stramenopiles, Telonemia, and Picozoa (figs. 1*B* and 2 and supplementary table S1, Supplementary Material online). We can rule out the possibility that these genes are actually derived from unnoticed viral infections or recent insertions of viral gene into nuclear genomes, as no evidence for such a possibility was found when checking the respective genome or transcriptome assemblies for hallmark *Nucleocytoviricota* genes. Furthermore, when genome data were available, eukaryotic *MidX* genes were usually found to contain introns (see supplementary table S1, Supplementary Material online), which are uncommon in viral genomes. Most of the MidX sequences obtained from metagenomes were closely related to sequences from taxonomically identified eukaryotic sources (fig. 2) and hence presumably originating from organisms affiliated to any of the five aforementioned lineages. Notably, we found several groups of extremely similar or identical *MidX* sequences coming from marine metagenomes from geographically different areas (fig. 2), indicating the global distribution of MidX-encoding organisms in marine environments.

All the *MidX* genes identified in previously recognized viral genomes (or fragments thereof) are assigned to the order *Imitervirales*, with nearly all of them representing the family *Mimiviridae* (see supplementary table S1, Supplementary Material online; using the most recent classification scheme; Aylward et al. 2021). Additional candidate viral *MidX* genes were represented by metagenomic sequences based on their phylogenetic relationship to known viral sequences (fig. 2). Inspection of the gene content of the respective genomic scaffolds provided independent evidence for the viral origin of these metagenomic sequences (except one, too short to be assigned to a specific biological source). While a more specific taxonomic assignment of these putative viral sequences is difficult to achieve, they generally retrieved genes from *Imitervirales* representatives as the best or only viral hits in blast searches, suggesting that MidX may be specific to this order among *Nucleocytoviricota*.

The internal topology of the MidX clade in both the "global" phylogeny of the dynamin superfamily (figs. 1*A* and S2, Supplementary Material online) and the tree restricted to MidX and Mgm1 (fig. 2) agreed on all the viral MidX sequences forming a monophyletic subgroup, although statistical support for this grouping (bootstrap value of 85%) was achieved only in the focused analysis. Furthermore, the viral MidX clade was nested in a paraphyletic assemblage of eukaryotic MidX sequences, although statistical support for the deepest branches in

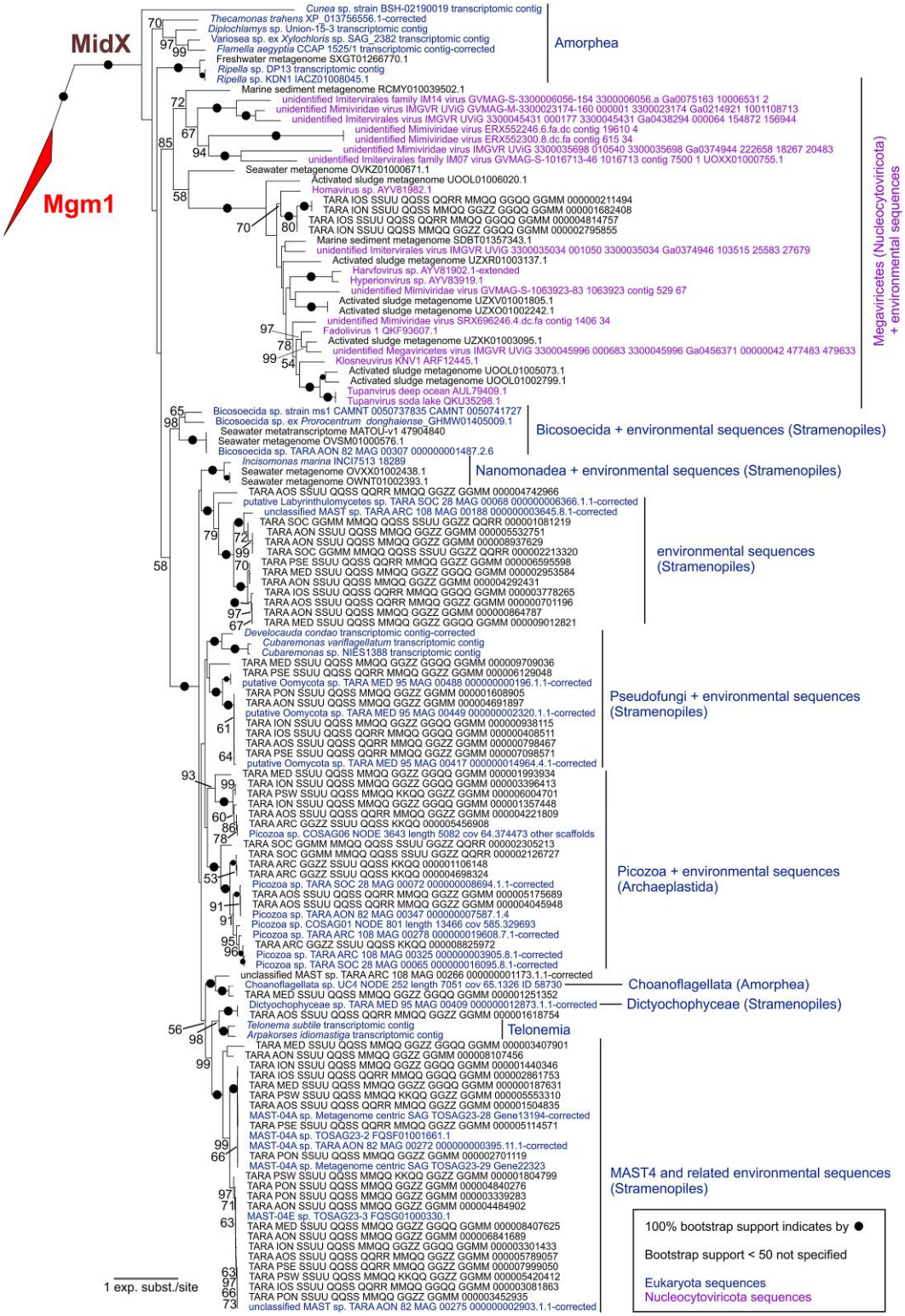

Fig. 2. Phylogenetic analysis MidX, a novel subgroup of the dynamin superfamily. The tree was inferred with the ML method in IQ-TREE (using the LG4X substitution model and 100 nonparametric bootstraps) based on a multiple sequence alignment of 583 positions. All nonredundant MidX sequences identified in various sequence resources were included, together with reference Mgm1 sequences used as an outgroup. The Mgm1 subtree is collapsed for simplicity (full version of the tree in supplementary fig. S3, Supplementary Material online). Color coding indicates sequences assigned to a specific eukaryotic or viral taxon as specified in the legend. Sequences in black are metagenomic or metatranscriptomic sequences that remain taxonomically unassigned.

the MidX clade was lacking in both analyses. At face value, the inferred MidX phylogenies indicate a single transfer of a *MidX* gene from a eukaryote to *Nucleocytoviricota*, perhaps an early member of *Imitervirales*. However, the specific eukaryote lineage that served as a donor cannot be deduced from the trees.

The interpretation of the evolutionary history of the MidX family is further complicated by the phylogenetic relationships of the eukaryotic *MidX* genes not closely following the known relationships of the source organisms themselves. For example, clusters of sequences from Picozoa and Telonemia, plus the single *MidX* gene identified in choanoflagellates, are nested in a fully supported large clade dominated by sequences from various subgroups of Stramenopiles. This topology is suggestive of horizontal transfer of *MidX* genes from stramenopile donors into the nonstramenopile lineages. Particularly notable is the *MidX* gene found in the single-cell genome assembly of a representative of an uncultured choanoflagellate lineage (sister to the order Acanthoecida; López-Escardó et al. 2019), which is a sole MidX representative within Opisthokonta, whose members normally contain Opa1 or Mgm1. An alternative explanation, that is, contamination, was not supported by a detailed inspection of the choanoflagellate genome assembly.

The discordance between the organismal and MidX gene phylogeny applies also to the relationships among stramenopile MidX sequences themselves, as they do not match our expectation based on the previously established stramenopile phylogeny. Namely, MidX sequences from Bicosoecida are expected to cluster with representatives from Nanomonadea, belonging to the same stramenopile clade Opalozoa (Azuma et al. 2022), but instead they branch outside the major stramenopile-dominated clade. Furthermore, MidX sequences from Amoebozoa (including a divergent sequence from an unidentified *Cunea* species that exhibited inconsistent behavior in different phylogenetic analyses; details in supplementary table S1, Supplementary Material online) are nonmonophyletic in our phylogenies and a subset of them is affiliated to a *MidX* gene from an apusomonad. Substantially improved sampling of MidX genes in the future may help to identify the reasons for the topological discordances discussed here, including a possible role of interlineage *MidX* gene transfer.

While the apparent specific relationship of MidX to Mgm1 and the predicted mitochondrial targeting of MidX proteins suggest that MidX may be functionally analogous to the well-characterized Mgm1, there is an important difference between the two protein groups: in contrast to Mgm1, which has a TMD in the region between the MTS and the GTPase domain (Herlan et al. 2003), no TMD was *in silico* predicted for any MidX protein using a standard prediction tool (Krogh et al. 2001). In fact, the region upstream of the first helix is shorter in most MidX proteins than the corresponding region in Mgm1 (see supplementary fig. S4, Supplementary Material online). Hence, MidX is clearly distinct from Mgm1 and the apparent lack of a TMD indicates it is not stably membrane-embedded. The architectural difference from Mgm1 also raised the question whether MidX reaches the intermembrane space or passes through the IMM to enter the mitochondrial matrix, which would be unprecedented for any known DRP.

Technical obstacles prevent us from answering this and other questions about MidX in its natural milieu, as none of the MidX-encoding eukaryotes is amenable to reverse genetics. Furthermore, of all the MidX-possessing viruses, only two have been isolated, Tupanvirus and Fadolivirus (Abrahão et al. 2018; Andreani et al. 2021), but it is unknown whether the amoebae used for their propagation in the lab are their natural hosts and if MidX is expressed in the respective culturing conditions. Thus, we resorted to examining the subcellular localization of a reference MidX protein in a heterologous cellular system, which allowed us to test the hypotheses that viral MidX is targeted to mitochondria and can remodel these organelles.

MidX Is Targeted to the Mitochondrial Matrix and Is Tightly Associated With the Inner Membrane

A *MidX* gene from *Hyperionvirus* (*HypMidX*) was selected as a representative of the newly discovered MidX clade due to the high probability of it having an MTS using several prediction programs (see supplementary table S1, Supplementary Material online), its unequivocal origin from a virus with an unambiguous placement within Mimiviridae family of *Nucleocytoviricota*, and the availability of a complete coding sequence. To experimentally confirm the predicted mitochondrial localization of MidX proteins, we generated a transgenic cell line of the kinetoplastid flagellate *Trypanosoma brucei* with a doxycycline-inducible expression of a synthesized codon-optimized version of the *HypMidX* gene fused to a region encoding a C-terminal V5 epitope tag. *Trypanosoma brucei* is an excellent model to study MidX because of its transgenic toolkit (Hashimi 2019) and its lack of Mgm1 or Opa1 orthologs that could possibly interfere with MidX in the mitochondrion.

We confirmed the mitochondrial targeting of HypMidX in two ways. Upon crude extraction of *T. brucei* mitochondria using the mild nonionic detergent digitonin, HypMidX-V5 was found in the same fraction as the mitochondrial marker mtHSP70, in contrast to the cytosolic enzyme enolase (fig. 3*A*). This result was confirmed by an indirect immunofluorescence assay, in which HypMidX-V5 colocalized with the mtHSP70 antibody signal early during doxycycline induction of *HypMidX* expression (fig. 3*B*).

To address into which mitochondrial subcompartment HypMidX-V5 was imported, mitoplasts (i.e., isolated mitochondria without an intact OMM) were subjected to a Proteinase K protection assay. The reproducible persistence of HypMidX-V5 signal upon Proteinase K treatment indicates that it is protected by the inner membrane and hence located within the matrix (fig. 3*C* and *D*). The retention of the matrix protein mtHSP70 and almost complete degradation of prohibitin, an integral inner membrane

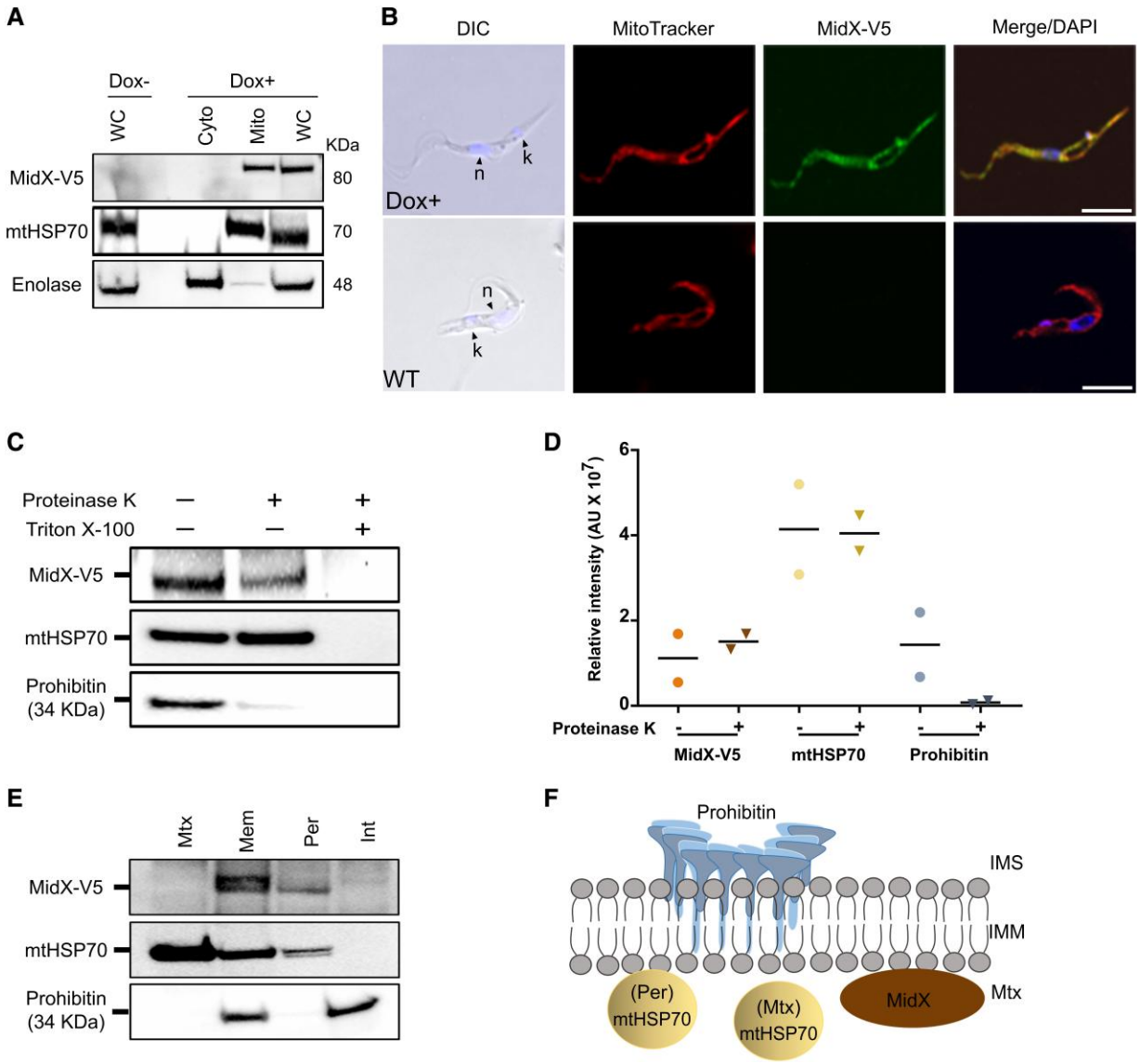

Fig. 3. HypMidX expressed in *T. brucei* is targeted into the mitochondrial matrix where it closely associates with the inner membrane. (*A*) Digitonin fractionation of procyclic *T. brucei* expressing HypMidX-V5. WC, whole cell; Cyto, cytoplasmic fraction; Mito, mitochondrial fraction; Dox; doxycycline. (*B*) Representative immunofluorescence confocal microscopy images of HypMidX-V5 expressing cells stained with MitoTracker Red marker (red) and anti-V5 antibody (green). Merged images show colocalization (yellow). Nucleus (n) and kinetoplast (k) stained by DAPI (blue) are indicated with arrowheads. Scale bar, 5 µm. (*C*) Proteinase K protection assay, in which mitoplasts were incubated with Proteinase K and Triton X-100 as indicated on top with "+." (*D*) Densitometric analysis of antibody intensities from biological duplicates of the Proteinase K protection assay depicted in (*C*). Horizontal bar shows mean of two signal intensities. (*E*) Carbonate extraction of mitochondria isolated from HypMidX-V5 expressing cells. Mtx, matrix; Mem, membrane; Per, peripheral membrane; Int, integral membrane. (*F*) A schematic summarizing HypMidX-V5 suborganellar localization results. IMS, intermembrane space; IMM, inner mitochondrial membrane; MTX, matrix.

protein that is mostly exposed within the intermembrane space, confirmed the functionality of the assay (fig. 3*C* and *D*). To further determine HypMidX-V5 localization, mitoplasts were separated into matrix and membrane fractions by repeated freeze/thaw lysis. The membrane fraction was processed into the integral and peripheral fractions. The veracity of these fractions was confirmed by detection of mtHSP70 in the matrix and peripheral IMM fractions, and prohibitin fractionating like an integral membrane protein (fig. 3*E*). Based on these immunoblot visualizations, we conclude that MidX associates with the matrix-facing leaflet of the IMM, as it cofractionates with mtHSP70, a peripheral IMM protein (fig. 3*E* and *F*).

MidX Dramatically Alters Mitochondrial Membranes in *T. brucei*

Our results thus unveil a new cellular niche for a dynamin superfamily protein that is—considering the consistent bioinformatics evidence—likely to hold for the other viral and eukaryotic MidX proteins in general. Previously characterized mitochondrial DRPs are associated with or

integrated into the OMM (Dnm1/DRP1 and mitofusins) or the IMM, yet with the bulk of the protein extruding into the intermembrane space (Opa1 and Mgm1). The association of MidX with the IMM from the matrix side is reminiscent of the localization of the distantly related dynamin superfamily protein called FZL, which associates with the inner plastid membrane from the stromal side in plants and green algae (Patil et al. 2018; Findinier et al. 2019). FZL regulates plastid and thylakoid morphology and promotes thylakoid fusion (Findinier et al. 2019). Hence, we wondered whether *HypMidX-V5* expression in the *T. brucei* stage that bears a canonical mitochondrion (Bílý et al. 2021) analogously affects mitochondrial morphology. The *HypMidX-V5* cell line was treated with doxycycline, and its growth over 6 days was compared with the same cell line cultured without the antibiotic. A progressively severe growth inhibition was observed (fig. 4A), which indicated that *HypMidX-V5* expression causes distress to the flagellate.

We next asked whether the observed growth inhibition may be caused by compromised mitochondrial physiology. Mitochondrial membrane potential is an indicator of the overall quality of the organelle, and this is measured by the accumulation of the tetramethylrhodamine ethyl ester (TMRE) dye in the matrix. Doxycycline induction of *HypMidX-V5* expression after 2 and 4 days resulted in a significant decrease in TMRE fluorescence compared with the "wild-type" (WT) parental cell line, indicating that *MidX* expression diminishes mitochondrial membrane potential in *T. brucei* (fig. 4B). WT cells were used as a control in subsequent experiments to mitigate potential leaky expression of *HypMidX-V5* in the absence of doxycycline.

We then studied MidX effects on the organelle's morphology. *T. brucei* expressing *HypMidX-V5* for 2 and 4 days was observed by indirect immunofluorescence using anti-mtHSP70 antibody to visualize gross mitochondrial morphology independent of membrane potential and quantify observed morphological phenotypes. The reticulated WT mitochondrion was predominantly altered into a tubular shape after 2 days of *HypMidX-V5* expression, with the majority of mitochondria apparently fragmented after 4 days (fig. 4C and D). Furthermore, the cell body exhibited an elongated appearance at both time points, likely due to the underlying morphological changes to the mitochondrion.

To better understand how MidX deforms mitochondrial ultrastructure, cells expressing *HypMidX-V5* for 4 days were observed by transmission electron microscopy (TEM) (fig. 4E). In sharp contrast to the typical slender profile of WT mitochondrial sections, whose matrices display a fine-grained electron density, the MidX-containing organelles were often expanded and relatively electron translucent. Interestingly, many of the mitochondrial sections contained double-membrane bound vesicles enclosing a compartment that resembled the electron density texture of the cytoplasm. These cytoplasmic pockets would presumably exclude matrix-targeted mtHSP70, explaining the fragmented appearance of the *T. brucei* mitochondrion visualized with anti-mtHSP70 antibody (fig. 4C).

While the 2D projection of TEM revealed a pronounced morphological phenotype in the mitochondrion, we could not conclusively address the nature of the intriguing double-membrane vesicles in *MidX*-expressing cells. Thus, we resorted to observing cells expressing *HypMidX-V5* for 4 days by volumetric serial block-face scanning electron microscopy (SBF–SEM) (Hughes et al. 2014). From a 200,000 μm^3 total volume, we selected for detailed analysis 30 cells whose entire volumes were captured by serial sectioning. We observed three main mitochondrial morphology phenotypes (fig. 5A) that occurred in various combinations: mitochondrial volume expansion (fig. 5B), cytoplasm protrusion into the mitochondrion (fig. 5C), and mitochondria with multilayered membranes, that is, the occurrence of more than two membranes (fig. 5D). The mitochondrial volume expansion (fig. 5B) and multilayered membranes in one mitochondrion (fig. 5D) appeared with similar frequency. These two phenotypes seem to be related to the most frequent one observed: cytoplasmic protrusion into the mitochondrion (fig. 5C). These cytoplasmic protrusions sometimes even included multiple peroxisome-related organelles called glycosomes (Moyersoen et al. 2004). The average diameter of a glycosome is between 270 and 300 nm (Tetley and Vickerman 1991), which is a testament to how voluminous the MidX-induced cytoplasmic protrusions can become.

One of the analyzed 30 cells showing all three phenotypes was reconstructed in 3D to obtain a representative image of MidX-induced remodeling of mitochondrial membranes (fig. 5E and F and supplementary movies S1 and S2, Supplementary Material online). The rendered mitochondrion had three bulbous structures, the largest of which (demarked with "a" in fig. 5E; see supplementary movies S1 and S2, Supplementary Material online) completely enclosed a 0.955 μm^3 volume of cytoplasm that included four glycosomes. In contrast to the example shown in figure 5C, the pocket contained by the bulb "a" is completely sealed off from the rest of the cytoplasm, while figure 5C shows protrusion that is still connected to the cytoplasm via a narrow channel. In any case, these protrusions are never observed in WT *T. brucei* cells. The two bulbs (fig. 5E and F and supplementary movie S2, Supplementary Material online) emerging near the nucleus showed expansion of the mitochondrial matrix with perhaps another glycosome (bulb "b"; putative glycosome demarked with asterisk in fig. 5F) or were comprised of multilayered membranes (bulb "c").

Thus, these observations support the notion that the *Hyperionvirus* MidX has the capacity to massively remodel mitochondrial membranes. We propose this holds for MidX proteins in general, including the eukaryotic ones. However, we acknowledge the drastic alteration of mitochondrial morphology seen *HypMidX*-expressing *T. brucei* is unlikely to reflect MidX's role in its natural physiological context. Indeed, mitochondria of the MidX-encoding eukaryotes that have been observed by TEM (*Thecamonas trahens*, telonemids, and *Ripella* sp.) exhibit standard morphology with tubulovesicular cristae

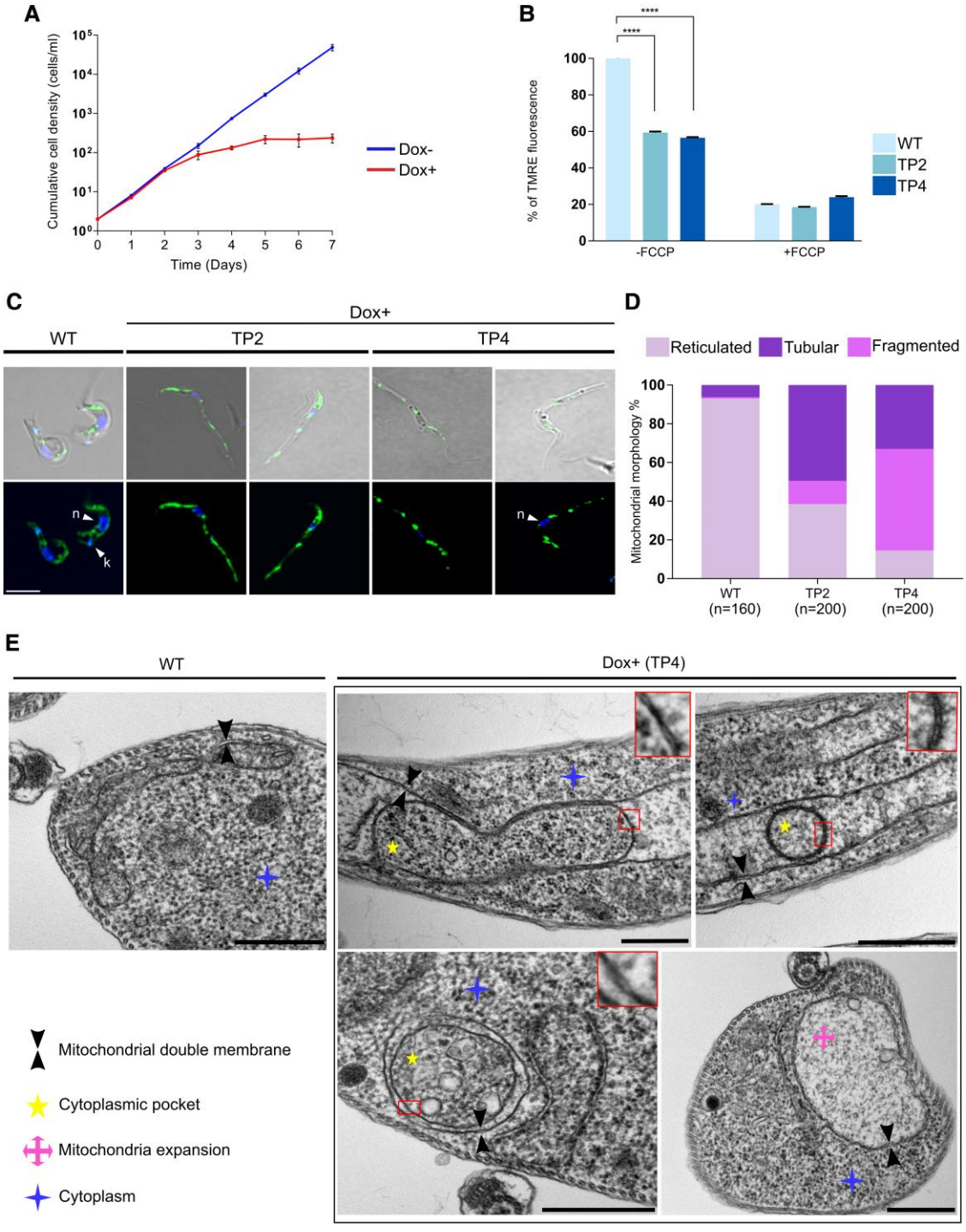

Fig. 4. HypMidX dramatically remodels the mitochondrion when expressed in *T. brucei*. (*A*) Effect of *HypMidX-V5* expression on *T. brucei* growth. Doxycycline-induced *HypMidX-V5* (Dox+) and noninduced (Dox−) shown in red and blue, respectively; standard deviations as whiskers. (*B*) Mitochondrial membrane potential measured by TMRE fluorescence after 2 (TP2) and 4 (TP4) days of doxycycline induction shown in a bar plot as percent of WT. Whiskers show standard deviation ($n = 3$). FCCP treatment displays complete membrane depolarization (****$P \leq 0.0001$). (*C*) Gross morphology of mitochondria as visualized by antibody against matrix-targeted mtHSP70 (green) in WT and TP2 and TP4 cells. Scale bar, 5 μm; k, kinetoplast; n, nucleus. (*D*) Quantification of mitochondrial morphology phenotypes in WT ($n = 160$) and TP2 and TP4 ($n = 200$) cells. Bars show proportion of cells exhibiting the normal reticulated (lightest purple) and defective tubular and fragmented (middle and darkest purple, respectively) morphologies. (*E*) Transmission electron micrographs of WT and TP4 cells. Regions in red boxes are magnified in insets at the upper right corner to highlight double membranes. Legend in the bottom left corner indicates symbols demarking normal and defective ultrastructures. Scale bar, 500 nm.

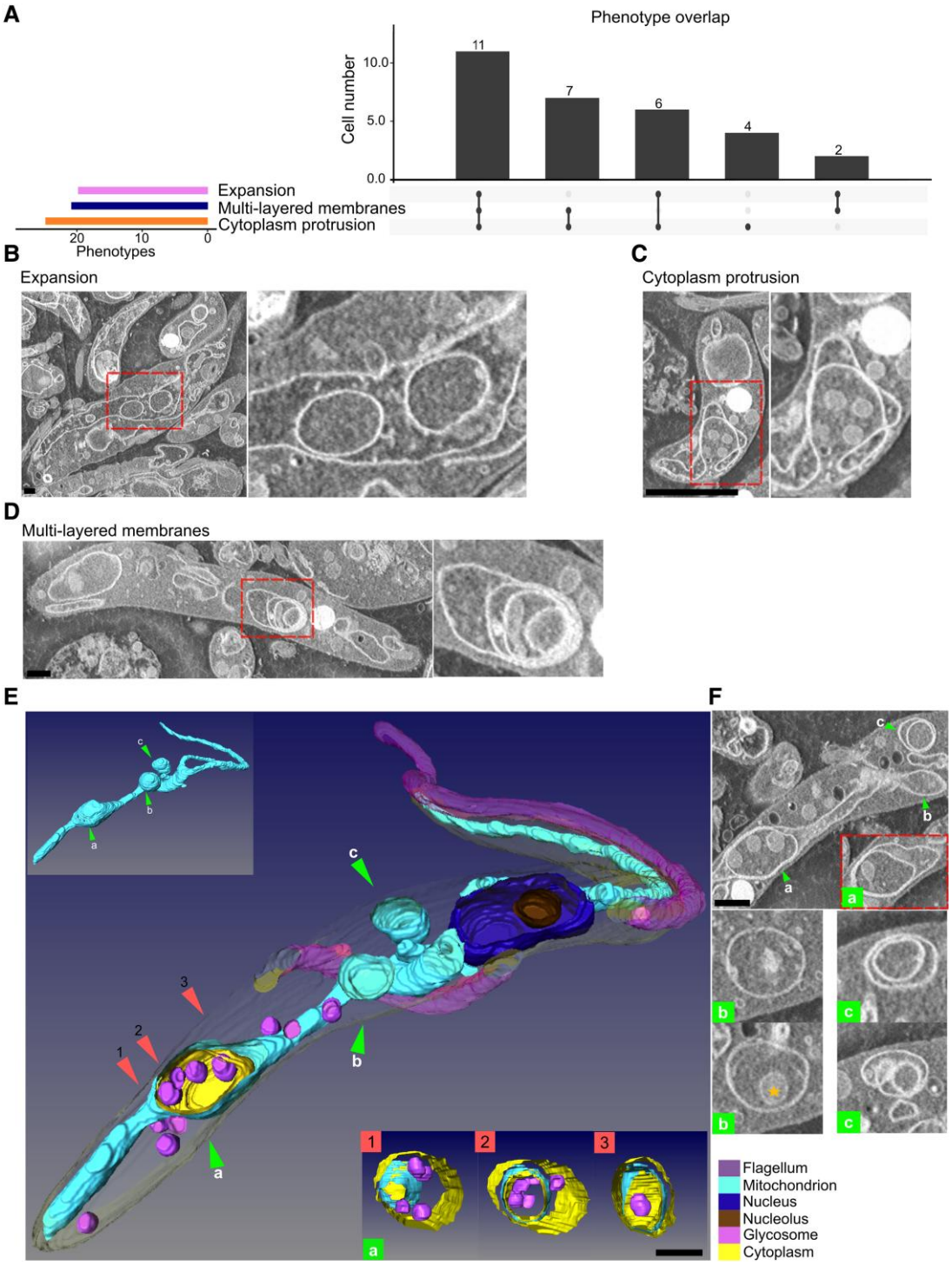

FIG. 5. Volumetric electron microscopy reveals that *HypMidX-V5* expression in *T. brucei* results in deformities to the mitochondria including cytoplasmic protrusions into the organelle. (*A*) Upset visualization quantifying the occurrence of three major mitochondrial morphology phenotypes ($n = 30$). The three phenotypes are represented in (*B*–*D*): mitochondrial volume expansion (*B*), cytoplasm protrusion into the mitochondrion (*C*, *D*), and mitochondria with multilayered membranes. (*E*) 3D reconstruction of a whole TP4 cell observed by SBF–SEM. The upper left corner shows the surface of the mitochondrion with indicated bulbous structures (green arrowheads). The central main image shows the cell with the uppermost layers trimmed to reveal the inside of these bulbs. Three images on the bottom right show crossvertical sections (labeled 1–3 with red arrowheads in the center image) of the mitochondrial bulb "a." (*F*) Raw SBF–SEM images showing serial sections through bulbs "a," "b," and "c" using the same labeling scheme. Scale bar, 1 μm. Related to supplementary movies S1 and S2, Supplementary Material online.

(Pánek et al. 2020; Tikhonenkov, Jamy, et al. 2022). It is conceivable that these organisms fine-tune MidX expression and/or possess regulators of the MidX function that avoid the detrimental impact of *HypMidX* expressed in the heterologous *T. brucei* system. Likewise, we do not expect that the expression of viral *MidX* in the natural hosts of the *MidX*-encoding *Nucleocytoviricota* would drastically remodel mitochondria, as this would likely not benefit viral replication. Perhaps the impact of MidX would be modulated by other proteins encoded by the viruses or specific adaptations possessed by the natural hosts. Hence, further characterization of the MidX proteins awaits the development of a suitable model system that recapitulates the natural milieu of *MidX*-expressing organisms. Nevertheless, we show here that MidX can remodel mitochondrial morphology from within the organelle's matrix, which is unprecedented for any DRP studied thus far.

Modeling Predicts Unique Structural Features of MidX Proteins

We attempted to gain additional insights into MidX function by taking advantage of the recent dramatic progress in protein structure modeling represented by AlphaFold2 (Jumper et al. 2021). Four de novo models of MidX proteins from *Hyperionvirus* (HypMidX) and three representatives of eukaryotes were highly similar to each other (figs. 6*A*, S5*A*–*D*, and S6, Supplementary Material online). This result along with the fact that AlphaFold2 model of *Saccharomyces cerevisiae* Mgm1 (see supplementary fig. S5*E*, Supplementary Material online) is consistent with the crystal structure of the protein (Yan et al. 2020) lent credence to the modeling results. MidX follows the general domain organization of other structurally characterized DRPs (fig. 6*B*), which feature a GTPase domain (G-domain) connected to a bundle signaling element (BSE) via hinge 2, which in turn is joined to the stalk by hinge 1. A variable domain (VD), sometimes referred to as a "paddle" (Faelber et al. 2019), was observed at the foot of the MidX structure. However, all four independently modeled MidX structures exhibited several striking features in comparison with Opa1, Mgm1, and the other modeled DRPs (figs. 6*A*, S5, and S6, Supplementary Material online).

First, all MidX models were in a closed (compacted) conformation, in which the stalk is folded against the G-domain by closure of the hinge 1. This closed confirmation was also observed when HypMidX was modeled as a dimer (fig. 6*B*). This is reminiscent of the conformation of the distantly related BDLPs (Low and Löwe 2006). Out of all eukaryotic DRPs, a closed conformation has been so far observed only in the crystal structure of the group A1 *Cyanidioschyzon merolae* CmDNM1 protein (Bohuszewicz and Low 2018). The closed conformation of CmDNM1 and BDLP were interpreted to represent the inactive, off-membrane state that presumably opens upon membrane binding and oligomerization of the protein (Low and Löwe 2006; Bohuszewicz and Low 2018). MidX possibly undergoes a similar conformational change depending on its association with IMM; thus, we cannot preclude that MidX assumes an open conformational state transiently even though AlphaFold2 exclusively predicts a closed conformation. It should be noted that AlphaFold2 models CmDNM1 in the same open conformation as seen in the other non-MidX DRPs (cf. supplementary figs. S5*O*, S5*P*, and S6*M*, Supplementary Material online), consistent with the idea that the CmDNM1 was captured in an inactive state. Notably, the angles at both hinges 1 and 2 differ between closed CmDNM1 and MidX, resulting in disparate conformations.

The second distinctive structural feature of MidX is that it is predicted with high confidence to lack a short helix contributing to the hinge 1 (figs. 6*C* and S6*A*, Supplementary Material online). Notably, this hinge 1 character is predicted in all four MidX models despite the disparity in amino acid sequences comprising this region (see supplementary fig. S6*Q*, Supplementary Material online). The apparent absence of this helix likely explains why the closed conformation is favored in the models. The third trait restricted to MidX is the organization of its VD. Unlike in other DRPs, in which VD is inserted between helices H3 and H4 of the stalk, the predicted MidX VD is comprised of two discontinuous segments, which are individually inserted between helices H1 and H2 and between helices H3 and H4 (fig. 6*A* and *B*). Perhaps as a consequence of this arrangement, the MidX VD is also rotated relative to the stalk compared with the VD of Mgm1 (fig. 6*D*). Thus, modeling of the MidX structure further underscores the plausible novelty of MidX among the DRPs studied so far.

The Discovery of MidX Obscures the Origin and Relationship of Opa1 and Mgm1

The discovery and characterization of MidX, while interesting in its own right, turned out to have broader evolutionary implications by changing the context for the interpretation of the origin and mutual relationship of two other mitochondrion-associated DRPs, Opa1 and Mgm1. These two DRPs share several traits and perform very similar function in remodeling the IMM (Pánek et al. 2020). This is consistent with previous analyses that detected Opa1 orthologs in Metazoa and their closest protist relatives, the choanoflagellates, representing the clade Holozoa, whereas Mgm1 was found to be Fungi-specific (Muñoz-Gómez et al. 2015). This complementary distribution in the two major lineages of the eukaryotic supergroup Opisthokonta leads to a natural hypothesis that Opa1 and Mgm1 are orthologs descended from a single gene present in the opisthokont common ancestor. Indeed, Opa1 and Mgm1 are presented as orthologs in a substantial portion of the literature dealing with these proteins (Faelber et al. 2019; Sinha and Manoj 2019; Zhang et al. 2020).

The results presented here challenge this interpretation. Firstly, our phylogenetic analyses using a comprehensive

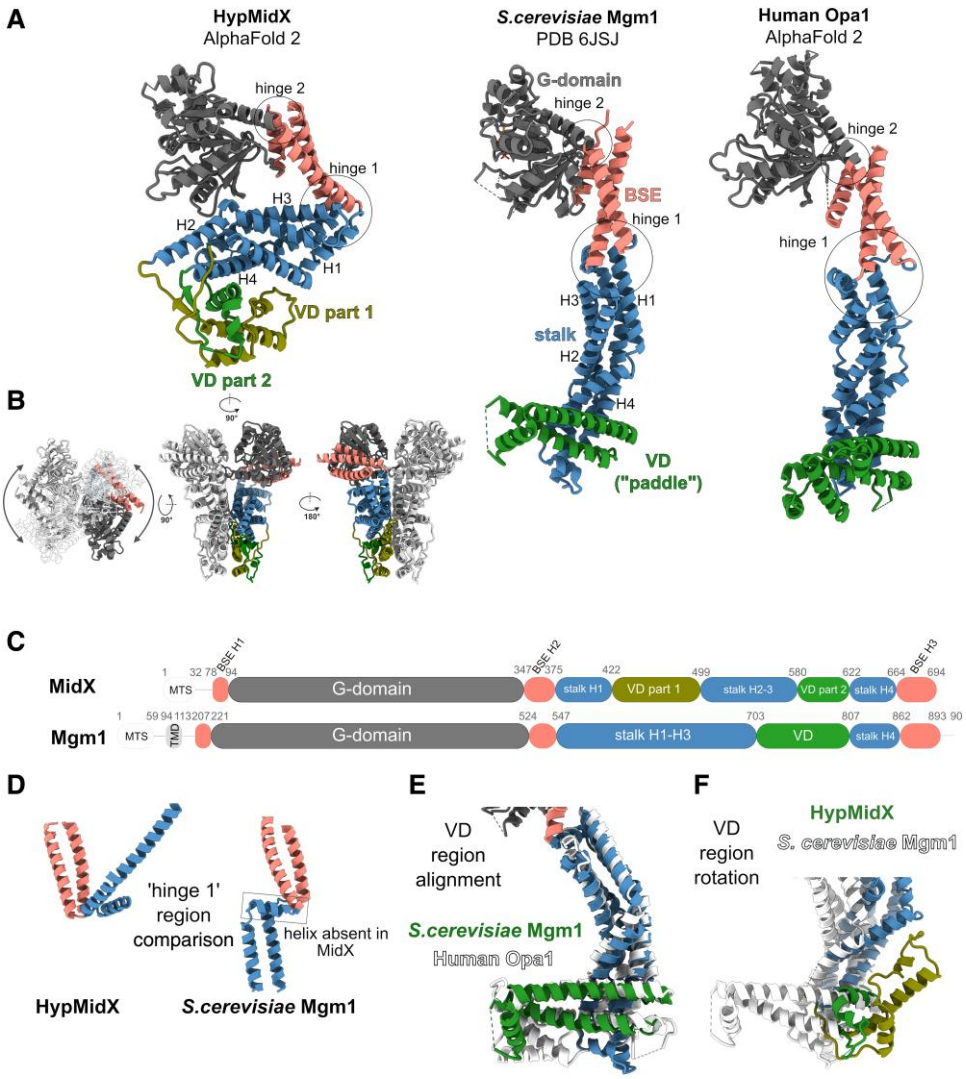

FIG. 6. MidX bears structural novelties that distinguish it from other dynamin superfamily proteins. (*A*) Structures of (from left to right) *Hyperionvirus* HypMidX (AlphaFold2 model), budding yeast Mgm1 (experimentally solved structure; Yan et al. 2020), and human Opa1 (AlphaFold2 model). The GTPase domain (G-domain), bundle signaling element (BSE), stalk (helices H1–4), and variable domain (VD, VD1, and VD2) color coding indicated on MidX and Mgm1 models. BSE-flanking hinge domains 1 and 2 are circled. (*B*) AlphaFold2 model of HypMidX dimers at the indicated orientations. One HypMidX monomer is colored as in (*A*). (*C*) DRP domains (amino acid coordinates above domain borders) mapped onto the primary structure of MidX (top) and Mgm1 (bottom). MTS, mitochondrial targeting signal; TMD, transmembrane domain. (*D*) Close-up of the hinge 1 regions of HypMidX and Mgm1, respectively, lacking or having the small alpha helix boxed onto Mgm1. (*E*) Structural alignment of the VDs of Mgm1 (white) and MidX (colored) showing relative rotation of the MidX VD. (*F*) Structural alignment of human Opa1 (white) and yeast Mgm1 (colored) VDs. The model segments with pLDDT scores <65 were neither interpreted nor depicted here.

data set of eukaryotic and viral DRPs never recovered a close relationship between Opa1 and Mgm1 (figs. 1A, S1, and S2, Supplementary Material online), consistent with other widescale phylogenetic analyses of DRPs (Purkanti and Thattai 2015; Sinha and Manoj 2019). Instead, Mgm1 consistently clustered together with MidX in our trees, albeit typically with weak statistical support. Opa1 sequences were always excluded from the MidX/Mgm1 clade, instead forming a monophyletic clade branching close to DRP group B3 and class C, albeit with considerably lower support than seen for the MidX/Mgm1 clade (fig. 1A). Crucially, this trend of Opa1 exclusion from the Mgm1/MidX clade was observed in other phylogenetic analyses that utilized sequences trimmed to the most conserved N-terminal part encompassing GTPase domain (supplementary fig. S1, Supplementary Material online). Thus, Mgm1 seems to have a closer phylogenetic relationship to MidX than to Opa1 based on conventional sequence-based phylogenetic analyses.

Secondly, even more compelling evidence indicating that Mgm1 and Opa1 are not necessarily orthologs is brought to light by an updated picture of the phylogenetic distribution of these two DRP types provided here (figs. 1B and S3 and supplementary table S2, Supplementary Material online). In the case of Mgm1, we demonstrate that in addition to Fungi and Rozellida, where it has

been reported before (Muñoz-Gómez et al. 2015), it also occurs in the closely related protist lineage Aphelidea, the representatives of Microsporidia that have preserved aerobic mitochondria, and certain representatives of Nucleariida. Thus, Mgm1 is a protein found in all major lineages of the Holomycota, one of the two major divisions of Opisthokonta (fig. 1*B*). The absence of Mgm1 from canonical Microsporidia characterized by highly reduced, genome-lacking mitochondria called mitosomes (Santos et al. 2018) and the nucleariid lineage represented by *Fonticula alba* and *Parvularia atlantis* can be explained by independent secondary losses. Whereas the extended taxonomic distribution of Mgm1 reported here is still perfectly compatible with the notion of Mgm1 and Opa1 being mutual orthologs specific for different major opisthokont subgroups, the wider than previously known distribution of Opa1 provided by our expanded sampling directly contradicts it: we found Opa1 not only in additional protist lineages of Holozoa (the second principal opisthokont subclade) but also in two representatives of the CRuMs supergroup, that is, a grouping external to opisthokonts (figs. 1*B* and S7, Supplementary Material online). (A few nonopisthokont DRPs assigned to Opa1 in another study (Sinha and Manoj 2019) were clearly misannotated; details in supplementary fig. S2, Supplementary Material online.) The monophyly of all Opa1 sequences including those from the CRuMs representatives is strongly supported (BS = 99 in the final analysis; see supplementary figs. S1*A* and S2, Supplementary Material online) and there is no evidence of contamination of the CRuMs transcriptome assemblies by sequences from holozoans, leaving no doubt on the existence of nonopisthokont *Opa1* genes.

The intertwined distribution pattern of Opa1, Mgm1, and MidX (fig. 1*B*) complicates hypothesizing about the origin of these mitochondria-shaping DRPs. The presence of MidX in representatives of the two eukaryote "megagroups" Diaphoretickes and Amorphea suggests it may have been present in early eukaryotes, possibly even the eukaryotic cenancestor, but later lost secondarily from most descendant lineages, notably including opisthokonts. The sole opisthokont *MidX* gene, identified in a single choanoflagellate, almost certainly represents a secondary gain by HGT. Notably, the genome sequence data available from this choanoflagellate do not indicate the presence of an *Opa1* gene, despite the fact that Opa1 is common in other choanoflagellates (see supplementary table S2, Supplementary Material online). It is possible that the putative MidX gain and the possible Opa1 loss in this choanoflagellate lineage are functionally connected, but we cannot rule out the possibility that the Opa1 absence is due to incompleteness of the genome data from the choanoflagellate (obtained as a single-cell genome assembly; López-Escardó et al. 2019). Regardless, at present, the occurrence of MidX and Opa1 or Mgm1 is mutually exclusive.

Two salient features of Mgm1 seem to lend themselves to an evolutionary scenario that Mgm1 is in fact a substantially modified MidX descendant: 1) the emergence of Mgm1 no later than in the ancestor of Holomycota (fig. 1*B*), that is, very early after the presumed loss of MidX in the opisthokont stem lineage, and 2) the phylogenetic evidence for the close relationship between Mgm1 and MidX. The phylogenetic position of Mgm1 outside rather than within the MidX clade in phylogenetic trees could then be explained as an artifact resulting from extensive sequence divergence of Mgm1 as the protein adapted to its new milieu. The discovery of CRuMs Opa1 (fig. 1*B*), together with the apparent phylogenetic separation between Opa1 and MidX/Mgm1, makes it possible that Opa1 coexisted with MidX in the common ancestor of CRuMs and Amorphea, with one or both DRP types later lost in different descendant lineages.

Unfortunately, the scenario outlined above relies on certain assumptions that are not necessarily valid and is even directly challenged by other considerations. The major argument against MidX being the ancestor of Mgm1 is that the former lacks the small alpha helix (fig. 6*B*) that is part of hinge 1 in all the diverse examined DRPs (see supplementary fig. S5, Supplementary Material online), implying it is an ancestral feature of eukaryotic DRPs. Furthermore, the VD domain of MidX is comprised of split motifs intertwined with the helices that constitute the stalk, another conspicuous deviation from other DRPs. Thus, the transformation of MidX into Mgm1 would require a reversion to an ancestral state, which contravenes the prevailing evolutionary trajectories of proteins. In fact, the hypothetical evolutionary transformation of MidX into Mgm1 would be a peculiar example of convergent evolution at the protein structure level, as the Mgm1 structure is strikingly similar to the modeled structure of the reference (human) Opa1 protein (fig. 6*A*), with some difference observed only in the VD region thanks to an extra short helix in Opa1 (fig. 6*E*). Nevertheless, the VD domains of Opa1 and Mgm1 are still remarkably similar, especially in comparison with MidX's VD domain (fig. 6*F*). Note that our AlphaFold2 Opa1 models are consistent with a low-resolution map of membrane-bound Opa1 oligomers (Zhang et al. 2020).

Furthermore, the inferred early origin of MidX and/or Opa1 may not necessarily be correct. The occurrence of these DRPs in distantly related lineages can also be a result of HGT rather than vertical inheritance from deep nodes of the eukaryote phylogeny. We have already discussed evidence for HGT of MidX from stramenopiles into telonemids, picozoans, and choanoflagellates, and the sporadic occurrence of MidX in Amorphea might also signal a HGT-derived origin of these genes. Similarly, HGT between Holozoa and CRuMs provides an alternative scenario to the hypothesis of the ancestral presence of Opa1 in the common ancestor of Amorphea and CRuMs. To test which scenario of Opa1 evolution is more likely, we performed a phylogenetic analysis restricted to Opa1 sequences to maximize the alignment length and hence the phylogenetic signal. As in the global DRP trees (see supplementary figs. S1 and S2, Supplementary Material online), the CRuMs sequences do not cluster together in the focused Opa1 phylogenetic analysis (see supplementary fig. S7, Supplementary Material online), which ostensibly

implies a specific evolutionary history including at least one HGT event. However, the phylogenetic resolution of the analysis remains limited, as evident from low branch support values and poor correspondence of the tree topology and the species relationships within Holozoa.

Ultimately, our efforts here did not yield an obvious and simple narrative about the coevolution of the mitochondrion and the dynamin superfamily. Convergence, HGT, recurrent loss, and/or extensive sequence divergence all seem to be ingredients of the story, but their exact role cannot be pinned down presently. Future methodological advances, new functional data on the different DRPs, and a more encompassing genome sampling of eukaryote diversity may eventually help resolve the current conundrum and answer the most salient question: why mitochondria of different lineages differentially employ MidX, Mgm1, or Opa1, and why so many other eukaryotes live happily without any of these DRPs?

To conclude, our analyses have established that viruses of the phylum *Nucleocytoviricota* frequently encode proteins from the dynamin superfamily, presumably as part of the battery of viral effectors modulating the physiology of the host cells to support viral reproduction. One subgroup of the viral DRPs is particularly interesting for belonging to a previously unnoticed group, denoted MidX, of mitochondrion-targeted DRPs sporadically present also in eukaryotes themselves. Our experiments support the hypothesis that MidX is a novel player in the mitochondrial membrane dynamics, although which specific aspects of the mitochondrial membrane biology are regulated by this protein and why only a few eukaryote lineages have retained (or acquired) it remain unclear. Nevertheless, the discovery of MidX is an important step in our quest to understand the evolutionary diversification of mitochondria, followed by the emergence of their key functional components. The data presented herein challenge the prevailing view in the field on the direct evolutionary correspondence of the metazoan Opa1 and the fungal Mgm1 proteins despite their ostensible functional and structural commonalities.

Materials and Methods

Building a Data Set of DRP Sequences

A combination of blastp searches against the NCBI nr database and sensitive homology detection using the HMMER3 package (Eddy 2011) were employed to search for homologs of DRPs. The HMMER3 tool was used to search a locally maintained protein sequence database (combining predicted proteins downloaded from public resources or inferred from nucleotide sequence data) in parallel to the recently reported EukProt database v02.2020 (Richter et al. 2022) and predicted proteins from *Nucleocytoviricota* isolates and MAGs (Moniruzzaman et al. 2020; Schulz et al. 2020). The searches employed, as a query, a profile HMM built based on a previously used seed multiple protein sequence alignment of eukaryotic DRPs (Karnkowska et al. 2019). Where appropriate or needed, profile HMMs were iteratively updated by expanding the template alignments with new homologs recognized in the previous search, especially with homologs of MidX and viral DRPs. Additional sequence resources, including metatranscriptomic and metagenomic assemblies from marine eukaryotes generated by the Tara Oceans project (Vorobev et al. 2020; Delmont et al. 2022), transcriptome and metagenome assemblies available at NCBI, the most recent version of EukProt (v03.2021), and viral sequences maintained in the IMG/VR database (Camargo et al. 2023), were searched with tblastn to identify additional MidX sequences. Predicted protein sequences of MidX obtained from eukaryotic (meta)genomes were manually curated to ensure that all exon–intron borders were identified correctly. Some truncated MidX/Mgm1/Opa1 transcripts were extended using reads from original sequencing data. For the final analyses, sequences were strategically subsampled to 593 proteins representing all main clades of DRPs in Eukaryota and *Nucleocytoviricota* as well as representatives of all main taxa.

Phylogenetic Analyses

Protein sequences were aligned using MAFFT version 7 using settings as follows: L-INS-i algorithm, gap opening penalty 1.3, leave gappy regions, and BLOSUM30 scoring matrix (Katoh and Standley 2013). To improve the final global DRP and Mgm1–MidX alignments, externally prepared alignment of experimentally determined of predicted structures of representatives from all main DRP groups, built with PROMALS3D program (Pei et al. 2008), was provided to the MAFFT aligner and used as a constraint. All alignments were trimmed manually (lengths of the trimmed alignments are indicated in the figure legends). Preliminary phylogenetic trees were built using FastTree 2 (Price et al. 2010) in an attempt to subsample representative eukaryotic DRPs prior our global analysis of DRPs. Final phylogenetic analyses were performed in IQ-TREE2 (Minh et al. 2020). All phylogenetic trees included in the final manuscript are based on the LG4X model (selected arbitrarily as a reasonably complex model given the size of the matrices fed into the phylogenetic analyses) with 100 or 200 nonparametric bootstraps. In the case of the global data set of the well-conserved N-terminal region of DRPs from eukaryotes and viruses (see supplementary fig. S1, Supplementary Material online), we also performed additional phylogenetic analyses using two complex and computationally demanding site-heterogeneous models, namely LG+C20+F+G4 and LG+C60+F+G4 (without bootstrapping).

In Silico Analyses of Protein Subcellular Targeting, TMDs, and Tertiary Structure

Subcellular localizations of viral DRPs and nonviral MidX sequences were predicted by using the following set of tools (run under default settings unless stated otherwise): TargetP v2 (Almagro Armenteros et al. 2019) in the "plant" setting, MultiLoc2 in animal and fungal settings (Blum et al. 2009), PProwler in nonplant setting (Hawkins and Bodén 2006), Predotar (Small et al. 2004) in the "animal

or fungal" setting, DeepMito (Savojardo et al. 2020), NommPred in mitochondria setting (Kume et al. 2018), MitoFates in "metazoa and fungi" settings (Fukasawa et al. 2015), and DeepLoc 2.0 (Thumuluri et al. 2022). The possible presence of transmembrane segments in MidX proteins was evaluated using TMHMM-2.0 (Krogh et al. 2001). Protein structures were predicted with AlphaFold2 (Jumper et al. 2021) using the ColabFold platform (Mirdita et al. 2022). The model segments with pLDDT scores <65 were neither interpreted nor depicted in figures. Models were visualized and figures prepared in ChimeraX (Pettersen et al. 2021).

Experimental Model Growth

The *T. brucei* procyclic form (RRID: SCR_004786), SmOxP strain 927 cell line used for transgenic experiments, was cultured at 27 °C in SDM79 medium supplemented with 10% (*v*/*v*) fetal bovine serum and 7.5 mg/L hemin as described previously (Kaurov et al. 2018). The cell culture was maintained at exponential growth phase. The *MidX* gene derived from *Hyperionvirus* (*HypMidX*, annotated as Hyperionvirus14_8 in the GenBank entry MK072396.1) was synthesized by General Biosystems, Inc. The amplicon was cloned into pT7-3xV5 vector (Flaspohler et al. 2010) with a hygromycin resistance marker. Subsequently, the construct was linearized by NotI and transfected as described before (Kaurov et al. 2018) into the SmOxP procyclic *T. brucei* cell line (Poon et al. 2012). Cells were grown in the absence and presence of 1 μg/mL doxycycline, which induced *HypMidX-V5* expression. Cell densities of induced and noninduced cultures were counted by the Beckman Coulter Z2 Cell and Particle Counter every 24 h. After every counting, cells were diluted to 2×10^6 cells/mL to maintain them in the exponential growth phase.

Digitonin Fractionation Assay, Proteinase K Protection Assay, and Carbonate Extraction Assay

For digitonin fractionation of organelles, 10^8 cells were used. The cell membrane was lysed in SoTE buffer (20 mM Tris-HCl, pH 7.5, 0.6 mL sorbitol, and 2 mM ethylenediaminetetraacetic acid), containing 0.015% (*w*/*v*) digitonin (D141-100MG, Sigma-Aldrich) for 5 min on ice. The suspension was centrifuged at 5,000 × g for 3 min at 4 °C to yield a mitochondria-enriched pellet and a supernatant enriched with cytosolic proteins (Bochud-Allemann and Schneider 2002). The digitonin-extracted mitochondria were also subjected to the Proteinase K protection assay which was done as previously described (Kaurov et al. 2018). Briefly, the mitochondria-enriched pellet was resuspended in SoTE supplemented with 0.2% (*w*/*v*) digitonin and incubated on ice for 15 min. After centrifugation as before, the resulting mitoplasts were resuspended in SoTE divided into three tubes: one treated with 50 μg Proteinase K; the second with Triton X 1% and Proteinase K; and the third remained untreated as a control. All samples were incubated on ice for 30 min and then 5 mM phenylmethylsulfonyl fluoride was added to each tube to stop the reaction. For carbonate extractions of integral membrane proteins, the procedure performed on hypotonically isolated mitochondria was done as previously (Kaurov et al. 2018). In brief, mitochondria resuspended in a 10 mM $MgCl_2$ solution were frozen in liquid nitrogen and thawed at room temperature (RT) for ten cycles. Then the suspension was centrifuged for 5 min at 10,000 × g at 4 °C. The supernatant and a portion of the pellet resuspended in 10 mM $MgCl_2$ was collected as the matrix and the membrane fraction, respectively. The rest of the pellet was resuspended in 0.1 M Na_2CO_3, incubated on ice for 10 min, and then centrifuged for 20 min at 100,000 × g at 4 °C. Then the supernatant was collected as the peripheral membrane protein fraction and the pellet was washed by resuspension in 0.1 M Na_2CO_3. The suspension was centrifuged for 20 min at 100,000 × g at 4 °C and the pellet was collected as the integral membrane protein fraction. All fractions of proteins were precipitated with trichloroacetic acid, resuspended in 0.1 M NaOH and then resolved by SDS–PAGE.

Mitochondrial Membrane Potential Measurement

Five million cells were resuspended in SDM-79 medium with 60 nM TMRE. After 30 min incubation at 27 °C, cells were spun down at 1,300 × g for 10 min at 27 °C. The cell pellet was resuspended in 1 mL of phosphate-buffered saline (PBS), pH 7.4, and immediately measured by fluorescence-activated cell sorting, collecting 10,000 events for each sample. Treatment with 20 μM of the ionophore carbonyl cyanide-p-trifluoromethoxyphenylhydrazone was used as a membrane potential uncoupling control.

Immunofluorescence Assay

Two million cells were incubated with 50 nM red-fluorescent stain MitoTracker Red for 30 min at 27 °C in SDM-79 medium. Cells were gently pelleted at 1,100 × g for 3 min at 27 °C. The pellet was resuspended in 4% (*w*/*v*) freshly made paraformaldehyde in PBS. After 1 h of incubation, the cells were centrifuged, and the pellet was resuspended in 100 μL of PBS. The suspension was applied to the superfrost slide. After 1 h of settling, the slide was washed with 0.1 M glycine and placed in 0.1% Triton X for 15 min. After washing three times with PBS, either polyclonal rabbit anti-V5 (1:200, Sigma) or monoclonal mouse anti-HSP70 (1:200) (Panigrahi et al. 2008) primary antibodies were applied to the slides. The slides were washed again three times with PBS and subsequently incubated in dark with goat anti-rabbit IgG Alexa 488 (H + L) (1:400) or goat anti-mouse IgG Alexa 488 (H + L) (1:400) secondary antibodies (Thermo Fisher). Finally, ProLong Gold Antifade Mountant with DAPI (Thermo Fisher) was applied on the slide and mounted with coverslip.

Transmission Electron Microscopy

For ultrastructural studies, cells were subjected to centrifugation at 620 × g for 10 min at 27 °C and then fixed with 2.5% glutaraldehyde in 0.1 M phosphate buffer, pH 7.2. Osmium tetroxide was used for postfixation at 4 °C for 2 h. Samples were then washed and dehydrated through

an acetone series and, finally, embedded in resin (Polybed 812; Polysciences, Inc.). A series of ultrathin sections were obtained by using a Leica UCT ultramicrotome (Leica Microsystems). Samples were counterstained with uranyl acetate and lead citrate. Observation was performed with a JEOL 1010 transmission electron microscope operating at an accelerating voltage of 80 kV which was equipped with a MegaView III charge-coupled device camera (Emsis).

SBF–SEM and 3D Reconstruction

Cell pellets were resuspended in a primary fixative containing 2.5% glutaraldehyde, 2% paraformaldehyde, and 2 mM $CaCl_2$ in 0.15 M cacodylate buffer. Pellets were incubated 30 min in 1% (*v*/*v*) tannic acid resuspended in 0.15 M cacodylate buffer supplemented with 2 mM CaCl and washed three times for 15 min with the same buffer. Pellets were embedded in 2% agarose and cut into small pieces. Samples were stained with modified OTO protocol (Deerinck et al. 2010) using the following steps (at RT and in water solution unless stated otherwise): 2% OsO_4 for 1.5 h, 2.5% ferrocyanide for 1.5 h, 1% thiocarbohydrazide for 2 h, 2% OsO_4 for 4 h, 1% uranyl acetate 12 h at 4 °C, and finally Walton Block for 2 h at 60 °C. In between each step, samples were washed three times for 15 min with H_2O. Dehydration was performed by acetone series containing 30%, 50%, 70%, 80%, 90%, 95%, and 100% acetone each for 15 min. Resin infiltration was carried using 1:2, 1:1, and 2:1 resin:acetone mixture, 1 h each step. Finally, samples were infiltrated in 100% resin 12 h and polymerized at 62 °C for 48 h. Samples embedded in the Hard Resin Plus 812 (EMS) were trimmed and imaged using an Apreo SEM (Thermo Fisher Scientific) equipped with the VolumeScope. The microscope acquisition settings were as follows: 3.5 kV, 80 pA, and low vacuum: 20 Pa. Serial images have a resolution of 6 nm (*X*, *Y*) and 65 nm in slice thickness (*Z*). In summary, an area of ~4,600 μm^2 on 668 slices was imaged resulting in the 200,000 μm^3 total sampled volume. Cells were processed, segmented, measured, and visualized in 3D using Microscopy Image Browser v2.702 (Belevich et al. 2016) and Amira v2020.2 (Thermo Fisher Scientific) softwares.

Statistical Analysis

All the statistical analysis was calculated by GraphPad Prism software, using an unpaired two-tailed Student's *t*-test. In this study, a *P* value of less than 0.05 was considered statistically significant. Upset visualization was performed by RStudio program (Lex et al. 2014).

Supplementary Material

Supplementary data are available at *Molecular Biology and Evolution* online.

Acknowledgments

This work was supported by the Czech Ministry of Education ERD Funds project OPVVV 16_013/0001775 and Czech Science Foundation grants 20-04150Y to O.G., 22-06479X to J.L., 20-27648S to M.E., and 20-23513S to H.H. The work of T.P. was supported by the Ministry of Education, Youth and Sports of the Czech Republic through the e-INFRA CZ (ID:90140) and by the Charles University Research Centre program no. 204069. We also acknowledge the support from Czech-BioImaging (LM2018129).

Data Availability

The MidX sequence from an undescribed variosean retrieved from an unpublished transcriptome assembly was deposited at GenBank with the accession number OQ924478.1. All other sequence analyses in this study come from publicly available resources (specified in supplementary tables S1 and S2, Supplementary Material online). Sequence alignments, phylogenetic trees in the NEWICK format, and structural models are available on the Figshare repository (10.6084/m9.figshare.22769669).

References

Abrahão J, Silva L, Silva LS, Khalil JYB, Rodrigues R, Arantes T, Assis F, Boratto P, Andrade M, Kroon EG, *et al.* 2018. Tailed giant Tupanvirus possesses the most complete translational apparatus of the known virosphere. *Nat Commun.* **9**:749.

Almagro Armenteros JJ, Salvatore M, Emanuelsson O, Winther O, von Heijne G, Elofsson A, Nielsen H. 2019. Detecting sequence signals in targeting peptides using deep learning. *Life Sci Alliance.* **2**:e201900429.

Anand R, Wai T, Baker MJ, Kladt N, Schauss AC, Rugarli E, Langer T. 2014. The i-AAA protease YME1L and OMA1 cleave OPA1 to balance mitochondrial fusion and fission. *J Cell Biol.* **204**:919–929.

Andreani J, Schulz F, Di Pinto F, Levasseur A, Woyke T, La Scola B. 2021. Morphological and genomic features of the new Klosneuvirinae isolate Fadolivirus IHUMI-VV54. *Front Microbiol.* **12**:719703.

Aylward FO, Moniruzzaman M, Ha AD, Koonin EV. 2021. A phylogenomic framework for charting the diversity and evolution of giant viruses. *PLoS Biol.* **19**:e3001430.

Azuma T, Pánek T, Tice AK, Kayama M, Kobayashi M, Miyashita H, Suzaki T, Yabuki A, Brown MW, Kamikawa R. 2022. An enigmatic stramenopile sheds light on early evolution in Ochrophyta plastid organellogenesis. *Mol Biol Evol.* **39**:msac065.

Belevich I, Joensuu M, Kumar D, Vihinen H, Jokitalo E. 2016. Microscopy image browser: a platform for segmentation and analysis of multidimensional datasets. *PLoS Biol.* **14**:e1002340.

Bílý T, Sheikh S, Mallet A, Bastin P, Pérez-Morga D, Lukeš J, Hashimi H. 2021. Ultrastructural changes of the mitochondrion during the life cycle of *Trypanosoma brucei*. *J Eukaryot Microbiol.* **68**:e12846.

Blum T, Briesemeister S, Kohlbacher O. 2009. MultiLoc2: integrating phylogeny and Gene Ontology terms improves subcellular protein localization prediction. *BMC Bioinformatics* **10**:274.

Bochud-Allemann N, Schneider A. 2002. Mitochondrial substrate level phosphorylation is essential for growth of procyclic *Trypanosoma brucei*. *J Biol Chem.* **277**:32849–32854.

Bohuszewicz O, Low HH. 2018. Structure of a mitochondrial fission dynamin in the closed conformation. *Nat Struct Mol Biol.* **25**:722–731.

Brahim Belhaouari D, Pires De Souza GA, Lamb DC, Kelly SL, Goldstone JV, Stegeman JJ, Colson P, La Scola B, Aherfi S. 2022. Metabolic arsenal of giant viruses: host hijack or self-use? *eLife* **11**:e78674.

Camargo AP, Nayfach S, Chen IMA, Palaniappan K, Ratner A, Chu K, Ritter Stephan J, Reddy TBK, Mukherjee S, Schulz F, *et al.* 2023. IMG/VR v4: an expanded database of uncultivated virus genomes within a framework of extensive functional, taxonomic, and ecological metadata. *Nucleic Acids Res.* **51**:D733–D743.

Da Cunha V, Gaia M, Ogata H, Jaillon O, Delmont TO, Forterre P. 2022. Giant viruses encode actin-related proteins. *Mol Biol Evol.* **39**:msac022.

Deerinck TJ, Bushong EA, Lev-Ram V, Shu X, Tsien RY, Ellisman MH. 2010. Enhancing serial block-face scanning electron microscopy to enable high resolution 3-D nanohistology of cells and tissues. *Microsc Microanal.* **16**:1138–1139.

Delmont TO, Gaia M, Hinsinger DD, Frémont P, Vanni C, Fernandez-Guerra A, Eren AM, Kourlaiev A, d'Agata L, Clayssen Q, *et al.* 2022. Functional repertoire convergence of distantly related eukaryotic plankton lineages abundant in the sunlit ocean. *Cell Genom.* **2**:100123.

Eddy SR. 2011. Accelerated profile HMM searches. *PLoS Comput Biol.* **7**:e1002195.

Faelber K, Dietrich L, Noel JK, Wollweber F, Pfitzner A-K, Mühleip A, Sánchez R, Kudryashev M, Chiaruttini N, Lilie H, *et al.* 2019. Structure and assembly of the mitochondrial membrane remodelling GTPase Mgm1. *Nature* **571**:429–433.

Findinier J, Delevoye C, Cohen MM. 2019. The dynamin-like protein Fzl promotes thylakoid fusion and resistance to light stress in *Chlamydomonas reinhardtii*. *PLoS Genet.* **15**:e1008047.

Fischer MG, Kelly I, Foster LJ, Suttle CA. 2014. The virion of *Cafeteria roenbergensis* virus (CroV) contains a complex suite of proteins for transcription and DNA repair. *Virology* **466–467**:82–94.

Flaspohler JA, Jensen BC, Saveria T, Kifer CT, Parsons M. 2010. A novel protein kinase localized to lipid droplets is required for droplet biogenesis in trypanosomes. *Eukaryot Cell* **9**:1702–1710.

Fukasawa Y, Tsuji J, Fu SC, Tomii K, Horton P, Imai K. 2015. MitoFates: improved prediction of mitochondrial targeting sequences and their cleavage sites. *Mol Cell Proteomics.* **14**:1113–1126.

Harper CB, Popoff MR, McCluskey A, Robinson PJ, Meunier FA. 2013. Targeting membrane trafficking in infection prophylaxis: dynamin inhibitors. *Trends Cell Biol.* **23**:90–101.

Hashimi H. 2019. A parasite's take on the evolutionary cell biology of MICOS. *PLoS Pathog.* **15**:e1008166.

Hawkins J, Bodén M. 2006. Detecting and sorting targeting peptides with neural networks and support vector machines. *J Bioinform Comput Biol.* **4**:1–18.

Herlan M, Vogel F, Bornhövd C, Neupert W, Reichert AS. 2003. Processing of Mgm1 by the rhomboid-type protease Pcp1 is required for maintenance of mitochondrial morphology and of mitochondrial DNA. *J Biol Chem.* **278**:27781–27788.

Hughes L, Hawes C, Monteith S, Vaughan S. 2014. Serial block face scanning electron microscopy—the future of cell ultrastructure imaging. *Protoplasma* **251**:395–401.

Imoto Y, Itoh K, Fujiki Y. 2020. Molecular basis of mitochondrial and peroxisomal division machineries. *Int J Mol Sci.* **21**:5452.

Jumper J, Evans R, Pritzel A, Green T, Figurnov M, Ronneberger O, Tunyasuvunakool K, Bates R, Žídek A, Potapenko A, *et al.* 2021. Highly accurate protein structure prediction with AlphaFold. *Nature* **596**:583–589.

Karnkowska A, Treitli SC, Brzoň O, Novák L, Vacek V, Soukal P, Barlow LD, Herman EK, Pipaliya SV, Pánek T, *et al.* 2019. The oxymonad genome displays canonical eukaryotic complexity in the absence of a mitochondrion. *Mol Biol Evol.* **36**:2292–2312.

Katoh K, Standley DM. 2013. MAFFT multiple sequence alignment software version 7: improvements in performance and usability. *Mol Biol Evol.* **30**:772–780.

Kaurov I, Vancová M, Schimanski B, Cadena LR, Heller J, Bílý T, Potěšil D, Eichenberger C, Bruce H, Oeljeklaus S, *et al.* 2018. The diverged trypanosome MICOS complex as a hub for mitochondrial cristae shaping and protein import. *Curr Biol.* **28**:3393–3407.e5.

Ketter E, Randall G. 2019. Virus impact on lipids and membranes. *Annu Rev Virol.* **6**:319–340.

Khalifeh D, Neveu E, Fasshauer D. 2022. Megaviruses contain various genes encoding for eukaryotic vesicle trafficking factors. *Traffic* **23**:414–425.

Kijima S, Delmont TO, Miyazaki U, Gaia M, Endo H, Ogata H. 2021. Discovery of viral myosin genes with complex evolutionary history within plankton. *Front Microbiol.* **12**:683294.

Koonin EV, Dolja VV, Krupovic M, Varsani A, Wolf YI, Yutin N, Zerbini FM, Kuhn JH. 2020. Global organization and proposed megataxonomy of the virus world. *Microbiol Mol Biol Rev.* **84**:e00061-19.

Koonin EV, Yutin N. 2019. Evolution of the large nucleocytoplasmic DNA viruses of eukaryotes and convergent origins of viral gigantism. Adv Virus Res. **103**:167–202.

Krogh A, Larsson B, von Heijne G, Sonnhammer ELL. 2001. Predicting transmembrane protein topology with a hidden Markov model: application to complete genomes. *J Mol Biol.* **305**:567–580.

Kume K, Amagasa T, Hashimoto T, Kitagawa H. 2018. NommPred: prediction of mitochondrial and mitochondrion-related organelle proteins of nonmodel organisms. *Evol Bioinform Online*. **14**:1176934318819835.

Kutsch M, Coers J. 2021. Human guanylate binding proteins: nanomachines orchestrating host defense. *FEBS J.* **288**:5826–5849.

Lex A, Gehlenborg N, Strobelt H, Vuillemot R, Pfister H. 2014. Upset: visualization of intersecting sets. *IEEE Trans Vis Comput Graph*. **20**:1983–1992.

López-Escardó D, Grau-Bové X, Guillaumet-Adkins A, Gut M, Sieracki ME, Ruiz-Trillo I. 2019. Reconstruction of protein domain evolution using single-cell amplified genomes of uncultured choanoflagellates sheds light on the origin of animals. *Philos Trans R Soc B Biol Sci.* **374**:20190088.

Low HH, Löwe J. 2006. A bacterial dynamin-like protein. *Nature* **444**:766–769.

Minh BQ, Schmidt HA, Chernomor O, Schrempf D, Woodhams MD, von Haeseler A, Lanfear R. 2020. IQ-TREE 2: new models and efficient methods for phylogenetic inference in the genomic era. *Mol Biol Evol.* **37**:1530–1534.

Mirdita M, Schütze K, Moriwaki Y, Heo L, Ovchinnikov S, Steinegger M. 2022. Colabfold: making protein folding accessible to all. *Nat Methods.* **19**:679–682.

Moniruzzaman M, Martinez-Gutierrez CA, Weinheimer AR, Aylward FO. 2020. Dynamic genome evolution and complex virocell metabolism of globally-distributed giant viruses. *Nat Commun.* **11**:1710.

Morales J, Ehret G, Poschmann G, Reinicke T, Maurya AK, Kröninger L, Zanini D, Wolters R, Kalyanaraman D, Krakovka M, *et al.* 2023. Host-symbiont interactions in *Angomonas deanei* include the evolution of a host-derived dynamin ring around the endosymbiont division site. *Curr Biol.* **33**:28–40.e27.

Moyersoen J, Choe J, Fan E, Hol WG, Michels PA. 2004. Biogenesis of peroxisomes and glycosomes: trypanosomatid glycosome assembly is a promising new drug target. *FEMS Microbiol Rev.* **28**:603–643.

Muñoz-Gómez SA, Slamovits CH, Dacks JB, Baier KA, Spencer KD, Wideman JG. 2015. Ancient homology of the mitochondrial contact site and cristae organizing system points to an endosymbiotic origin of mitochondrial cristae. *Curr Biol.* **25**:1489–1495.

Pánek T, Eliáš M, Vancová M, Lukeš J, Hashimi H. 2020. Returning to the fold for lessons in mitochondrial crista diversity and evolution. *Curr Biol.* **30**:R575–R588.

Panigrahi AK, Zíková A, Dalley RA, Acestor N, Ogata Y, Anupama A, Myler PJ, Stuart KD. 2008. Mitochondrial complexes in *Trypanosoma brucei*: a novel complex and a unique oxidoreductase complex. *Mol Cell Proteomics.* **7**:534–545.

Patil M, Seifert S, Seiler F, Soll J, Schwenkert S. 2018. FZL is primarily localized to the inner chloroplast membrane however influences thylakoid maintenance. *Plant Mol Biol.* **97**:421–433.

Pei J, Kim B-H, Grishin NV. 2008. PROMALS3D: a tool for multiple protein sequence and structure alignments. *Nucleic Acids Res.* **36**:2295–2300.

Pernas L, Scorrano L. 2016. Mito-morphosis: mitochondrial fusion, fission, and cristae remodeling as key mediators of cellular function. *Annu Rev Physiol.* **78**:505–531.
Pettersen EF, Goddard TD, Huang CC, Meng EC, Couch GS, Croll TI, Morris JH, Ferrin TE. 2021. UCSF ChimeraX: structure visualization for researchers, educators, and developers. *Protein Sci.* **30**:70–82.
Poon SK, Peacock L, Gibson W, Gull K, Kelly S. 2012. A modular and optimized single marker system for generating *Trypanosoma brucei* cell lines expressing T7 RNA polymerase and the tetracycline repressor. *Open Biol.* **2**:110037.
Praefcke GJK, McMahon HT. 2004. The dynamin superfamily: universal membrane tubulation and fission molecules? *Nat Rev Mol Cell Biol.* **5**:133–147.
Price MN, Dehal PS, Arkin AP. 2010. Fasttree 2—approximately maximum-likelihood trees for large alignments. *PLoS One* **5**:e9490.
Purkanti R, Thattai M. 2015. Ancient dynamin segments capture early stages of host–mitochondrial integration. *Proc Natl Acad Sci USA.* **112**:2800–2805.
Ramachandran R, Schmid SL. 2018. The dynamin superfamily. *Curr Biol.* **28**:R411–R416.
Richter DJ, Berney C, Strassert JFH, Poh Y-P, Herman EK, Muñoz-Gómez SA, Wideman JG, Burki F, de Vargas C. 2022. EukProt: a database of genome-scale predicted proteins across the diversity of eukaryotes. *Peer Community J.* **2**:e56.
Rodrigues RAL, de Souza FG, de Azevedo BL, da Silva LCF, Abrahão JS. 2021. The morphogenesis of different giant viruses as additional evidence for a common origin of Nucleocytoviricota. *Curr Opin Virol.* **49**:102–110.
Rolland C, Andreani J, Sahmi-Bounsiar D, Krupovic M, La Scola B, Levasseur A. 2021. Clandestinovirus: a giant virus with chromatin proteins and a potential to manipulate the cell cycle of its host *Vermamoeba vermiformis*. *Front Microbiol.* **12**:715608.
Rout MP, Field MC. 2017. The evolution of organellar coat complexes and organization of the eukaryotic cell. *Annu Rev Biochem.* **86**:637–657.
Santos HJ, Makiuchi T, Nozaki T. 2018. Reinventing an organelle: the reduced mitochondrion in parasitic protists. *Trends Parasitol.* **34**:1038–1055.
Savojardo C, Bruciaferri N, Tartari G, Martelli PL, Casadio R. 2020. DeepMito: accurate prediction of protein sub-mitochondrial localization using convolutional neural networks. *Bioinformatics* **36**:56–64.
Schulz F, Abergel C, Woyke T. 2022. Giant virus biology and diversity in the era of genome-resolved metagenomics. *Nat Rev Microbiol.* **20**:721–736.
Schulz F, Roux S, Paez-Espino D, Jungbluth S, Walsh DA, Denef VJ, McMahon KD, Konstantinidis KT, Eloe-Fadrosh EA, Kyrpides NC, *et al.* 2020. Giant virus diversity and host interactions through global metagenomics. *Nature* **578**:432–436.
Sinha S, Manoj N. 2019. Molecular evolution of proteins mediating mitochondrial fission–fusion dynamics. *FEBS Lett.* **593**:703–718.
Small I, Peeters N, Legeai F, Lurin C. 2004. Predotar: a tool for rapidly screening proteomes for N-terminal targeting sequences. *Proteomics* **4**:1581–1590.
Tetley L, Vickerman K. 1991. The glycosomes of trypanosomes: number and distribution as revealed by electron spectroscopic imaging and 3-D reconstruction. *J Microsc.* **162**:83–90.
Thumuluri V, Almagro Armenteros JJ, Johansen Alexander R, Nielsen H, Winther O. 2022. DeepLoc 2.0: multi-label subcellular localization prediction using protein language models. *Nucleic Acids Res.* **50**:W228–W234.
Tice AK, Žihala D, Pánek T, Jones RE, Salomaki ED, Nenarokov S, Burki F, Eliáš M, Eme L, Roger AJ, *et al.* 2021. PhyloFisher: a phylogenomic package for resolving eukaryotic relationships. *PLoS Biol.* **19**:e3001365.
Tikhonenkov DV, Jamy M, Borodina AS, Belyaev AO, Zagumyonnyi DG, Prokina KI, Mylnikov AP, Burki F, Karpov SA. 2022. On the origin of TSAR: morphology, diversity and phylogeny of Telonemia. *Open Biol.* **12**:210325.
Tikhonenkov DV, Mikhailov KV, Gawryluk RMR, Belyaev AO, Mathur V, Karpov SA, Zagumyonnyi DG, Borodina AS, Prokina KI, Mylnikov AP, *et al.* 2022. Microbial predators form a new supergroup of eukaryotes. *Nature* **612**:714–719.
Vorobev A, Dupouy M, Carradec Q, Delmont TO, Annamalé A, Wincker P, Pelletier E. 2020. Transcriptome reconstruction and functional analysis of eukaryotic marine plankton communities via high-throughput metagenomics and metatranscriptomics. *Genome Res.* **30**:647–659.
Wolf DM, Segawa M, Kondadi AK, Anand R, Bailey ST, Reichert AS, van der Bliek AM, Shackelford DB, Liesa M, Shirihai OS. 2019. Individual cristae within the same mitochondrion display different membrane potentials and are functionally independent. *EMBO J.* **38**:e101056.
Yan L, Qi Y, Ricketson D, Li L, Subramanian K, Zhao J, Yu C, Wu L, Sarsam R, Wong M, *et al.* 2020. Structural analysis of a trimeric assembly of the mitochondrial dynamin-like GTPase Mgm1. *Proc Natl Acad Sci USA.* **117**:4061–4070.
Zhang D, Zhang Y, Ma J, Zhu C, Niu T, Chen W, Pang X, Zhai Y, Sun F. 2020. Cryo-EM structures of S-OPA1 reveal its interactions with membrane and changes upon nucleotide binding. *eLife* **9**:e50294.